Chapter 2

Turbulent Flow of Viscoelastic Fluid Through Complicated Geometry

Takahiro Tsukahara and Yasuo Kawaguchi

Additional information is available at the end of the chapter

http://dx.doi.org/10.5772/52049

1. Introduction

Viscoelastic liquids with very small amounts of polymer/surfactant additives can, as well known since B.A. Toms' observation in 1948, provide substantial reductions in frictional drag of wall-bounded turbulence relative to the corresponding Newtonian fluid flow. Friction reductions of up to 80% compared to the pure water flow can be occasionally achieved with smooth channel/pipe flow of viscoelastic surfactant solution [11, 54]. This friction-reducing effect, referred to as turbulent drag reduction (DR) or Toms effect, has been identified as an efficient technology for a large variety of applications, e.g. oil pipelines [25] and heating/cooling systems for buildings [43], because of major benefits in reducing energy consumption.

It has been known that long, high-molecular-weight, flexible polymers or rod-like micelle networks of surfactant are particularly efficient turbulence suppressor, so that those solutions lead to different turbulent states both qualitatively and quantitatively, resulting in dramatic DRs. One of promising additives, which may allow their solutions to induce DR, is a cationic surfactant such as "cetyltrimethyl ammonium chloride (CTAC)" under appropriate conditions of surfactant chemical structure, concentration, counter-ion, and temperature to form micellar networks in the surfactant solution. Those resulting micro-structures give rise to viscoelasticity in the liquid solution. The properties and characteristics of the viscoelastic fluids measured even in simple shear or extensional flows are known to exhibit appreciably different from those of the pure solvent. From a phenomenological perspective, their turbulent flow is also peculiar as is characterized by extremely elongated streaky structures with less bursting events. Therefore, the viscoelastic turbulence has attracted much attention of researchers during past 60 years. Intensive analytical, experimental, and numerical works have been well documented and many comprehensive reviews are available dealing with this topic: [cf., 18, 19, 26, 35, 51, , and others].

Although the mechanism of DR is still imperfectly understood, but some physical insights have emerged. In particular, with the aid of recent advanced supercomputers, direct

numerical simulations (DNSs) of viscoelastic fluid as well as the Newtonian fluid have been increasingly performed [e.g., 1, 7, 17, 41, 44]. Some progresses in the model of DR and in the understanding of modulated turbulent structures have been made by L'vov et al. [20] and Roy et al. [39]. Later, Kim et al. [16] carried out DNS to examine interactions between the coherent structures and the fluid viscoelasticity. They reported a dependency of the vortex-strength threshold for the auto-generation of new hairpin vortices in the buffer layer on the viscoelasticity. Most of DNS studies in the literature are performed on flows over smooth wall surface and other simple flow configurations, such as channel flow, boundary layer, isotropic turbulence, and shear-driven turbulence.

As well as smooth turbulent flows in plane channel and pipe, the turbulent flow through complex geometries has both fundamental scientific interest and numerous practical applications: such flows are associated with the chemical, pharmaceutical, food processing, and biomedical engineering, where the analysis and designing for their pipe-flow systems are more difficult than for its Newtonian counterpart. This is mainly because severe limitations in the application of ideal and Newtonian flow theories to these relevant flow problems. Most of the previous work presented in the literature concerning this subject has been done with flows either through sudden expansion or over backward-facing step. The flow even in such relatively simple cases of complex geometries exhibits important features that partain to complex flows containing flow separation, reattachment, and often an extremely high level of turbulence. A better understanding of viscoelastic-fluid behavior and turbulent flow properties of those flows should lead to both the design and the development of hydrodynamically more efficient processes in various pipe-flow systems and to an improved quality control of the final products. Consequently, in situations of both practical and fundamental importance, we have investigated the detailed mechanism and efficiency of DR for viscoelastic turbulent flow through roughened channel, or an orifice flow, that is one of canonical flows involving separation and reattachment. The goal of a series of our works is to better understand the physics of viscoelastic turbulent flow in complicated flow geometry.

The following subsections give a brief introduction to the preceding studies that motivated us to further investigate the viscoelastic turbulent orifice flow and describe the more specific purpose of the study reported in this chapter.

1.1. Related studies

As far as we know there exist no other DNS studies on the viscoelastic turbulent orifice flow than those carried out by authors' group recently. However, there are a few experimental and numerical works on sudden expansion and backward-facing step owing to their geometrical simplicity. Table 1 summarizes several earlier works.

As for the Newtonian fluid, Makino et al. [22, 23] carried out DNSs of the turbulent orifice flow, and investigated also the performance of heat transfer behind the orifice. They reported several differences in turbulent statistics between the orifice flow and other flows of the sudden expansion and the backward-facing step. Recently, the authors' group investigated the viscoelastic fluid in the channel with the same rectangular orifice using DNS [46, 49]. We found phenomenologically that the fluid viscoelasticity affected on various turbulent motions in just downstream of the orifice and attenuated spanwise vortices.

By means of experiments, we confirmed the turbulence suppression in the region behind the orifice and analyzed the flow modulation with respect to the turbulent structures by

Configuration	Author(s)	Method	Expansion ratio
Orifice	Present	Sim.	1:2
	Tsurumi et al. [50]	Exp.	1:2
Sudden expansion	Pak et al. [29]	Exp.	1:2, 3:8
	Castro & Pinho [3]	Exp.	1:1.54
	Escudier & Smith [8]	Exp.	1:1.54
	Poole & Escudier [32, 33]	Exp.	1:2, 1:4
	Oliveira [28]	Sim.	1:2
	Manica & De Bortoli [21]	Sim.	1:3
	Dales et al. [5]	Exp.	1:1.5
	Poole et al. [34]	Sim.	1:3
Backward-facing step	Poole & Escudier [31]	Exp.	1:1.43

Table 1. Relevant previous studies on viscoelastic turbulent flow: Exp., experiment; Sim., numerical simulation.

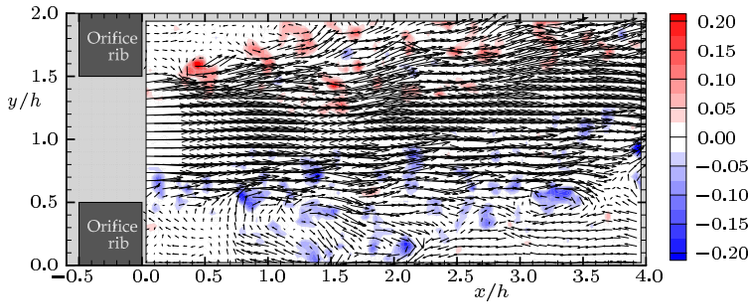

(a) Water

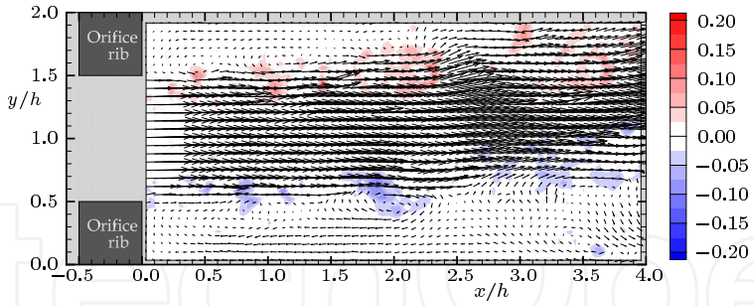

(b) CTAC, 150 ppm

Figure 1. Snapshots of flow fields behind the orifice, taken by PIV measurement: vector, (u, v); contour, the swirling strength $\lambda_{ci}\omega_z/|\omega_z|$ (positive, anti-clockwise rotation; negative, clockwise). The main flow direction is from left to right. Cited from [50].

using PIV (particle image velocimetry) [50]. Figure 1 shows the instantaneous velocity vectors in a plane of interest. Also shown is the contour of swirling strength, by which the vortex core can be extracted by plotting iso-surface of $\lambda_{ci} > 0$, the imaginary part of complex conjugate eigenvalue of velocity-gradient tensor in the two-dimensional plane, and the rotational direction be evaluated by the sign of spanwise rotation ω_z. As can be seen in the figure, the sudden expansion of the orifice leads to generation of strong separated shear layers just behind the orifice-rib edges. This shear layer enhances turbulence dominantly

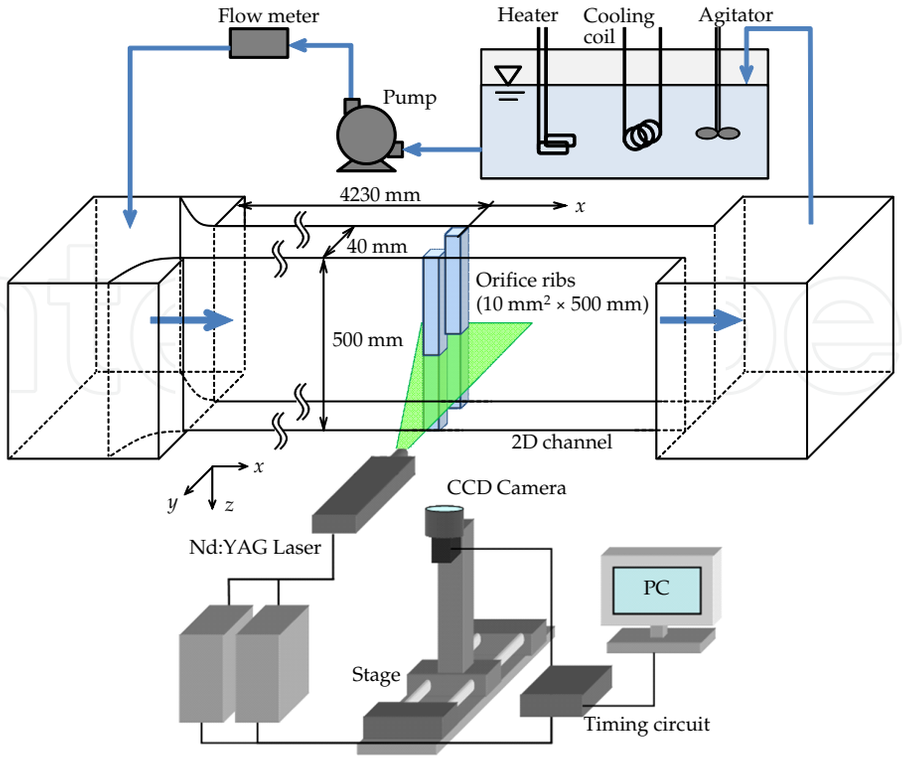

Figure 2. Outline of experimental apparatus with PIV system.

in the water flow, while the viscoelastic flow seems rather calm. Here, the viscoelastic fluid they employed was the CTAC solution with 150 ppm of weight concentration. A schematic of the experimental set up is depicted in Fig. 2. The Reynolds number based on the actual bulk mean velocity passing the orifice were $Re_{\mathrm{m}} = 8150$ for water and 7840 for the viscoelastic fluid (CTAC solution), which were obtained under the same pumping power. It is interesting to note that the hydrodynamic drag throughout the channel including the orifice is rather increased in the viscoelastic flow despite the presence of turbulence-suppression phenomenon. We conjectured that, in the experiment, any DR did not apparently occur because an increment of the skin friction by an extra shear stress due to viscoelasticity exceeded a decrement of the Reynolds shear stress. It might be difficult to determine the individual contribution of either turbulence, viscosity, or viscoelasticity in such an experimental study. To achieve clearer pictures of the role of viscoelasticity and turbulence modulations affecting on DR, we should re-examine the viscoelastic turbulent orifice flow with emphasis on the viscoelastic force (stress) exerted on the fluctuating flow motion.

1.2. Purpose

In the present study, we will focus on an instantaneous field of the viscoelastic turbulent flow past the rectangular orifice and discuss mainly the interaction between the turbulent fluid motion and the (polymer/surfactant) additive conformation field, i.e. the balance of the inertia, viscous, and viscoelastic forcing terms in the governing momentum equation. We have made some preliminary studies which have shown that this flow exhibits a change in the augmentation of the local heat transfer dependently on the streamwise distance from the orifice [49]. Therefore, we propose in this chapter that this streamwise variation of

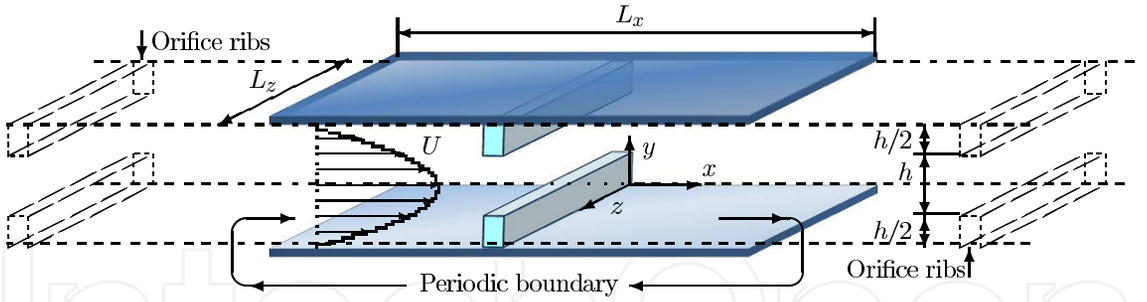

Figure 3. Configuration of the roughened-channel flow for the simulation, where a sequence of regularly-spaced, rectangular, orifices is considered.

the heat-transfer augmentation would be deeply related to the turbulence-viscoelasticity interaction, and suggest its scenario.

We performed DNSs without any turbulence model but with the Giesekus' viscoelastic-fluid model, valid for a polymer/surfactant solution, which is generally capable of reducing the turbulent frictional drag in a smooth channel. The geometry considered here is periodic orifices with the 1:2 expansion ratio.

2. Problem formulation

In this section, the equations governing incompressible viscoelastic-fluid flows are presented in their dimensional and non-dimensional forms. Rheological properties relating to a model we employed here to calculate the polymer/surfactant, or the fluid-viscoelasticity, contribution to the extra-stress tensor are also described.

2.1. Flow configuration

Prior to introducing the equations, let us depict the configuration of the computational domain in Fig. 3. In the three dimensional Cartesian coordinate system, x, y, and z indicate the streamwise, wall-normal, and spanwise directions, respectively. The main flow is driven by the streamwise mean pressure gradient. The flow that we analyzed by DNS was assumed to be fully-developed turbulent flow through an obstructed channel, of height $L_y = 2h$, with periodically repeating two-dimensional orifices (i.e., transverse rectangular orifices): namely, in the simulations, the periodic boundary condition was adopted in the x direction as well as the z direction to allow us to demonstrate an infinite channel and regularly-spaced obstructions Note that, by contrast with the above-mentioned experiment, where transient flows past only one orifice were studied, we numerically investigated the fully-developed flows through a sequence of orifices. As illustrated in Fig. 3, the transverse orifices are placed in every L_x in the x direction.

The height of each rib is chosen as $0.5h$—the channel half height is h—and thus the expansion ratio of the orifice is 1:2, that is equivalent to the experimental condition but the thickness in the x direction is small as $0.1h$. These present conditions relating to the orifice installation are the same as those studied by Makino et al. [22]. The no-slip boundary condition is used on all the wall surfaces including the faces of the orifice.

The domain size in the streamwise direction ($L_x = 12.8h$) was not sufficiently long that the effects of the orifice on the flow approaching next one could be neglected. The domain size

along the spanwise direction was chosen as $L_z = 6.4h$, which was confirmed to be adequate based on the convergence of the spanwise correlation to almost zero at this domain size.

2.2. Governing equations

In this study, the governing equations for the three velocity components $\mathbf{u} = \{u, v, w\}$ and pressure p take the form:

$$\nabla \cdot \mathbf{u} = 0, \tag{1}$$

$$\rho \frac{\mathrm{D}\mathbf{u}}{\mathrm{D}t} = -\nabla p + \eta_\mathrm{s} \nabla^2 \mathbf{u} + \nabla \cdot \boldsymbol{\tau}_\mathrm{p}, \tag{2}$$

with t the time, ρ the fluid density, and η_s the Newtonian-solvent viscosity. These fluid properties are assumed to be constant, irrespective of the flow fields. In the last term, there exists an additional stress-tensor component $\boldsymbol{\tau}_\mathrm{p}$, which is related with kinematic quantities by an appropriate constitutive equation. A model which has proved effective in reproducing a power-law region for viscosity and normal-stress coefficients as well as a reasonable description of the elongational viscosity for viscoelastic surfactant solutions was proposed by Giesekus [10]. This model assumes that the extra stress $\boldsymbol{\tau}_\mathrm{p}$ due to additives in the solution satisfies

$$\boldsymbol{\tau}_\mathrm{p} + \lambda \overset{\triangledown}{\boldsymbol{\tau}}_\mathrm{p} + \alpha \frac{\lambda}{\eta_\mathrm{a}} \left(\boldsymbol{\tau}_\mathrm{p} \cdot \boldsymbol{\tau}_\mathrm{p} \right) = 2\eta_\mathrm{a} \mathbf{S}, \tag{3}$$

where λ is the relaxation times, $\overset{\triangledown}{\boldsymbol{\tau}}_\mathrm{p}$ is the upper convected derivative of the stress tensor, and $\mathbf{S}$ is the deformation tensor. The parameter η_a has dimensions of viscosity (but note that η_a represents the additive contribution to the zero-shear-rate solution viscosity: $\eta_0 = \eta_\mathrm{s} + \eta_\mathrm{a}$). For the mobility parameter representing magnitude of the non-linearity of the fluid elasticity, $\alpha = 0.001$ was given as our previous studies [45, 46, 52, 53].

From several kinds of the non-Newtonian fluid model, such as FENE-P model and Oldroyd-B model, we chose the Giesekus model to properly resolve the evolution of extra stress due to the deformation of macromolecules in the surfactant solution. One can find in the literature [14, 42] that measured rheological properties of the surfactant solution agree well with those of a Giesekus fluid.

To re-write Equations (2) and (3) in their non-dimensional forms, we should introduce a dimensionless conformation tensor $\mathbf{c} = c_{ij}$ given by an explicit function of

$$\boldsymbol{\tau}_\mathrm{p} = \frac{\eta_\mathrm{a}}{\lambda} \left(\mathbf{c} - \mathbf{I} \right). \tag{4}$$

and derive the dimensionless forms as follows:

$$\frac{\partial u_i^+}{\partial t^*} + u_j^+ \frac{\partial u_i^+}{\partial x_j^*} = -\frac{\partial p^+}{\partial x_i^*} + \frac{\beta}{Re_{\tau 0}} \frac{\partial^2 u_i^+}{\partial {x_j^*}^2} + \frac{1-\beta}{We_{\tau 0}} \frac{\partial c_{ij}}{\partial x_j^*} + F_i, \tag{5}$$

and

$$\frac{\partial c_{ij}}{\partial t^*} + u_k^+ \frac{\partial c_{ij}}{\partial x_k^*} - \frac{\partial u_i^+}{\partial x_k^*} c_{kj} - c_{ik} \frac{\partial u_j^+}{\partial x_k^*} + \frac{Re_{\tau 0}}{We_{\tau 0}} \left[c_{ij} - \delta_{ij} + \alpha \left(c_{ik} - \delta_{ik} \right) \left(c_{kj} - \delta_{kj} \right) \right] = 0. \tag{6}$$

Quantities with a superscript, $\square^+$, indicate that they are normalized by the friction velocity $u_{\tau 0}$, that is given by the force balance between the wall shear stress and the mean pressure

gradient through the computational volume in the case of the plane channel without any orifice nor obstruction, i.e.,

$$u_{\tau 0} = \sqrt{\frac{\tau_{w0}}{\rho}} = \sqrt{-\frac{\delta}{\rho} \cdot \frac{\Delta p}{L_x}}. \tag{7}$$

Here, τ_{w0} is the averaged wall shear stress for a smooth plane channel flow and Δp is the time-averaged pressure drop between $x = -L_x/2$ and $L_x/2$. The other superscript, or $\square^*$, represents non-dimensionalization by the channel half width: e.g., $x^* = x/h$. As for the three non-dimensional parameters of $Re_{\tau 0}$, $We_{\tau 0}$, and β, their definitions and specific values will be described in Section 2.3

In order to mimic the solid body of the orifice in the fluid flow, the direct-forcing immersed boundary method [9, 24] was applied on the surface of the orifice ribs and their inside. The additional term of F_i in Equation (5) represents the body force vector per unit volume for this method.

2.3. Rheological and flow parameters

We executed two simulations of the orifice flows for either viscoelastic fluid or Newtonian fluid, for comparison. All present DNSs were run under a constant pressure drop: $\Delta p/L_x$ was constant and it enabled us to define a constant friction Reynolds number $Re_{\tau 0} = \rho u_{\tau 0} h/\eta_0$. In this work, $Re_{\tau 0}$ was fixed at 100 for each simulation. The friction Weissenberg number representing the ratio between the relaxation time and the viscous time scale was chosen to be $We_{\tau 0} = \rho \lambda u_{\tau 0}^2/\eta_0 = 20$ in the viscoelastic flow. The viscosity ratio of the solvent viscosity to the solution viscosity at a state of zero shear stress was taken as $\beta = \eta_s/\eta_0 = 0.8$. These rheological conditions would provide a noticeable drag-reducing effect to turbulent flows in a smooth channel. Actually, our previous DNS result that pertained to the similar condition ($Re_{\tau 0} = 150$, $We_{\tau 0} = 10$, and $\beta = 0.8$) provided a moderate drag reduction more than 10% [45]. As for the Newtonian fluid, these parameters corresponds to $We_{\tau 0} = 0$ and $\beta = 1$, which leads to Equation (5) in the common form for the Newtonian fluid.

In our previous works [46, 49], while the friction Reynolds number and the Weissenberg number were ranged, respectively, from 100 to 200 and from 0 to 30, the drag reduction rates of 15–20% were achieved in the viscoelastic flows. Unfortunately, to the authors' knowledge, there has never been any other DNS study of viscoelastic turbulent orifice flow, partly due to numerical difficulty, namely, the Hadamard instability [12] in viscoelastic-flow calculations.

3. Numerical procedure

3.1. spatial discretization

The finite difference method was adopted for the spatial discretization. Two different grid numbers of $256 \times 128 \times 128$ and $128 \times 128 \times 128$ in (x, y, z) were used for the Newtonian and the viscoelastic flows, respectively, since the Newtonian turbulent flow is basically accompanied by finer eddies that need to be resolved. For the coarser mesh, the spatial resolutions were $\Delta x^+ = 10$ and $\Delta z^+ = 5$ with the computational domain size of $L_x \times L_y \times L_z = 12.8h \times 2h \times 6.4h$ and were reasonable to capture flow variations and small-scale eddies behind the orifice. According to the results shown later, the orifice flow of the viscoelastic fluid indeed has exhibited relatively-large turbulent structures and offered reasonable statistics. In

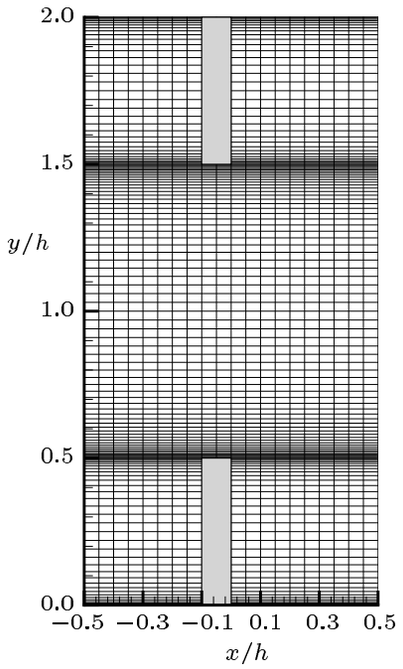

Figure 4. Computational grids with emphasis on the orifice ribs, viewed from the spanwise direction.

the wall-normal direction, the density of the computational mesh is not uniform so that dense grids appear at the height of the orifice rib and near the walls, as shown in Fig. 4. Using a hyperbolic tangent stretching factor, we employed the resolutions of $\Delta y^+ = 0.31$–3.01.

In the x and z directions, the central difference scheme with the 4th-order accuracy was employed, while the 2nd-order accuracy was in the y direction. It should be noted, however, that the 'minmod' flux-limiter scheme as a TVD (total-variation diminishing) method was adopted to the non-linear term in Equation (6): details of this numerical method can be found in the authors' papers [48, 52].

3.2. Time integration

The SMAC (simplified marker and cell) method was applied for coupling between Equations (1) and (5); and the time advancement was carried out by the 3rd-order Runge-Kutta (RK) scheme, but the 2nd-order Crank-Nicolson scheme was used for the viscous term in the y direction, although of course several alternatives to these methods for the coupling and time integration may be available. Regarding the issue to ensure proper methods, we preliminarily tested a variety of combinations with the same flow geometry and conditions and evaluated their availability with emphasis on the orifice rib. Before showing this verification result, let us note again that we employed the immersed-boundary technique for the orifice ribs, or the rigid solid phase in fluid circumstance. The idea of this technique, firstly proposed by Peskin [30], is to employ a regular Cartesian grid, but to apply additional suitable momentum source within the domain in order to satisfy the requisite conditions at the interface and inside of the solid phase [36]. In the present simulation with the Cartesian grid, the velocities defined either at the surface or the inside of the orifice ribs were required to be zero. Hence, we should appropriately calculate the additional term F_i in Equation (5) to drive those velocities to the desired value, when compute the set of the governing equations. We examined two coupling methods—the SMAC method

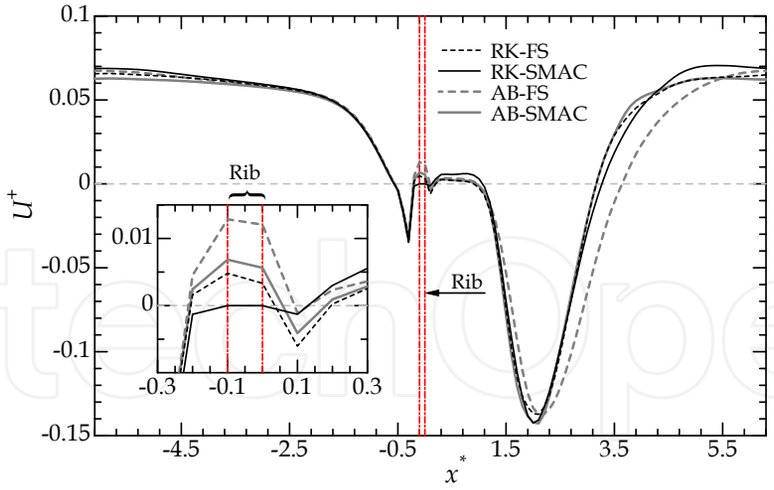

Figure 5. Dependence on numerical methods: streamwise distribution of a velocity in the vicinity of the upper wall for the Newtonian-fluid flow at $Re_{\tau 0} = 100$.

and the fractional-step (FS) method—and two time-integration scheme—the RK scheme and the 2nd-order Adams-Bashforth (AB) scheme. Figure 5 compares the results obtained by the different combinations of them. We choose to show only the curves for the near-wall distribution of the mean streamwise velocity, U^+ at $y^* = 0.0053$ ($y^+ = 0.53$) from the upper wall. Focusing on the location of the rib, you can find considerable variability of the value dependently on the scheme combination: see the inset of Fig. 5. As might be expected, the RK scheme with higher accuracy gave near-zero U at the rib, indicating a better performance than the AB scheme. Moreover, the marked reduction in the U pertaining to the SMAC method can be also clearly seen. It reflects the fact that, when combined with appropriate choice of coupling method and time-integration scheme, this immersed-boundary method leads to a reasonable simulation.

One may observe other locations where scheme-dependent variability seems to be significant. For instance, the reattachment point at which the near-wall U changes its sign was apparently found to vary according to numerical schemes, as seen in Figure 5. This might be true, but a large deviation of the reattachment point by the combination of AB and SMAC is attributed to a straightening phenomena in the mean flow, which is essentially bended to one wall by the Coanda effect. Although not shown in figure, the same verification of U in the core region was also done, but revealed no remarkable variation between different methods at every streamwise position. It implies that the scheme-dependency can be ignorable except for the near-wall region at the orifice. The undesirable non-zero U through the rib in the case of AB-FS is thought of as a main reason for the weaken Coanda effect and the straightened flow.

In the following, instantaneous flow fields and several turbulence statistics obtained by the DNS with RK-SMAC are shown.

4. Results

4.1. Instantaneous flow field: Kelvin-Helmholtz and turbulent eddies

A major difference between the present study and published works on the smooth channel is related to the streamwise variation of the flow state and the main turbulence-producing

area. Although the flow past an orifice is one of the simplest reattaching flows, the flow field is still very complex compared to the smooth channel flow. The contracted flow passing the orifice detaches at its leading edge, forming a separated shear layer. Even if the the contracted flow is laminar-like, transition begins soon after separation unless the Reynolds number is very low as $Re_{\mathrm{m}} < 400$ for the backward-facing step flow [2, 27] and the same orifice flow [22]. The present bulk Reynolds numbers as low as $Re_{\mathrm{m}} = 579$ and 646 for the Newtonian and viscoelastic flows, respectively, exceed this critical value and are in the transitional regime. As a consequence of the increase in Re_{m}, the viscoelastic flow is determined as it offers a lower drag by about 20%, which corresponds to the 'drag reduction rate.' Most of drag-reduced turbulent flows over smooth wall differ from the Newtonian flows in the same general way [51]: for instance, the fluid viscoelasticity inhibits transfer of kinetic energy from the streamwise to the wall-normal velocity fluctuations, and vorticity fluctuations inducing production of turbulence in near-wall region disappear in the highly drag-reduced flow, even as the bulk Reynolds number is raised from that for the Newtonian flow with the same pressure drop. In these contexts, the instantaneous vortex structures both within the strong shear layer just downstream of the orifice and in the downstream after the reattachment point should be of interest for investigation of viscoelastic-fluid behaviors. Actually, the DNS study on the turbulent heat transfer [49] demonstrated a heat-transfer augmentation in the region of $x > 6h$ (i.e., area after the reattachment) even with drag reduction, when compared with the Newtonian case: we will discuss again regarding this phenomenon in Section 5.3.

Figure 6 presents an instantaneous snapshot of eddies in each of the Newtonian flow and viscoelastic flow, viewed three-dimensionally with emphasis on the orifice downstream. Here, eddies are visualized by the second invariant of the fluctuating velocity-gradient tensor:

$$II' = \frac{\partial u_i'}{\partial x_j}\frac{\partial u_j'}{\partial x_i}. \tag{8}$$

Additionally, the contours in the figures show the instantaneous streamwise velocity ($u = U + u'$) distribution in an arbitrary x-y plane and its distribution near the bottom wall, revealing the adverse flow region just behind the orifice and high and low momentum patches on the wall surface below eddies. The orifice flows presented in Fig. 6 are highly unsteady and turbulent in region behind the orifice for both fluids. However, the viscoelastic flow seems to involve turbulent structures very similar to those in the Newtonian flow, but the number of eddies is drastically reduced. The spanwise vortices, especially Kelvin-Helmholtz (K-H) vortices, in the strong shear layer released from the orifice edge are less remarkable, which is qualitatively consistent with the experimental observation mentioned in Section 1. This vortex suppression phenomenon is expected to be induced by the viscoelasticity.

It is interesting to note that the near-wall streaks becomes highly intermittent but still occurs in the region far downstream of the reattachment point. The mean reattachment point locates at $x = 4.3h$ on the lower-side wall surface. Because of the bulk Reynolds number as low as 650, it is naturally expected that no apparent turbulent eddies should not be observed in far-downstream region away from the orifice, where the flow would be laminar similar to the smooth channel flow at the same Reynolds number. However, as can be seen in the figure, the velocity distributions both of the Newtonian and the viscoelastic flows are far from those in the laminar state. In particular, the viscoelastic flow exhibits larger vortices far from the orifice: elongated longitudinal vortical structures are observed intermittently at $x = 5$–$7h$, as given in Fig. 6(b). Those large-scale structures may induce velocity fluctuations and also

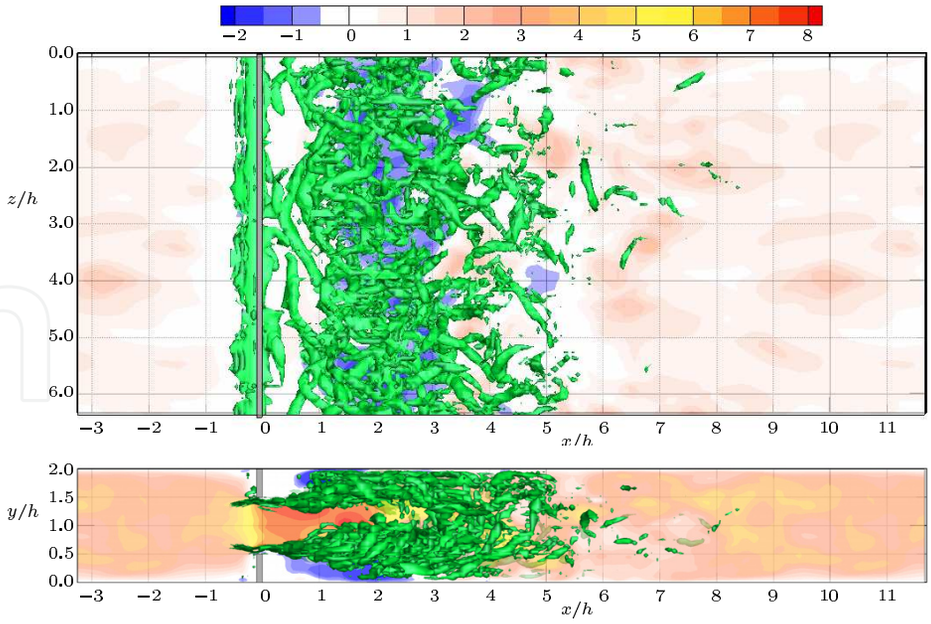

(a) Newtonian fluid

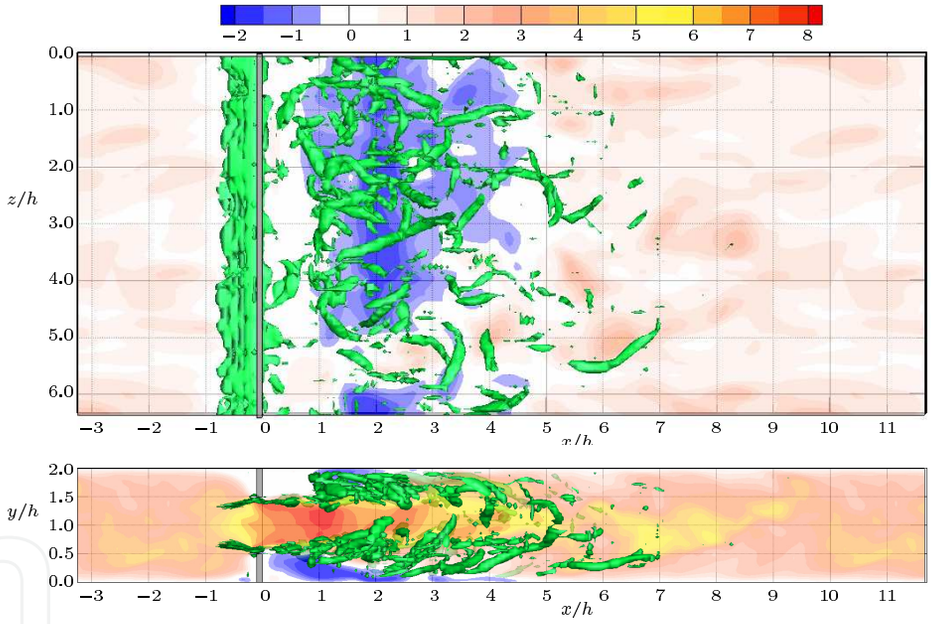

(b) Viscoelastic fluid

Figure 6. Visualized instantaneous flow fields of the obstructed turbulent channel flows. Green iso-surfaces indicate negative regions of the second invariant of the deformation tensor, representing vortical structures. The contours show instantaneous streamwise velocity distribution in an arbitrary x-y plane and in the x-z plane at $y^* = 0.05$ from the lower wall.

significant transports of momentum/heat between the near-wall region and the core region. As demonstrated later (in Section 4.2), the near-wall sweep/ejection motions that pertain to longitudinal vortex are prone to be encouraged by the viscoelastic force. Therefore, it can be conjectured that instability due to the viscoelastic process causes velocity fluctuations as well as vortices in the far downstream region.

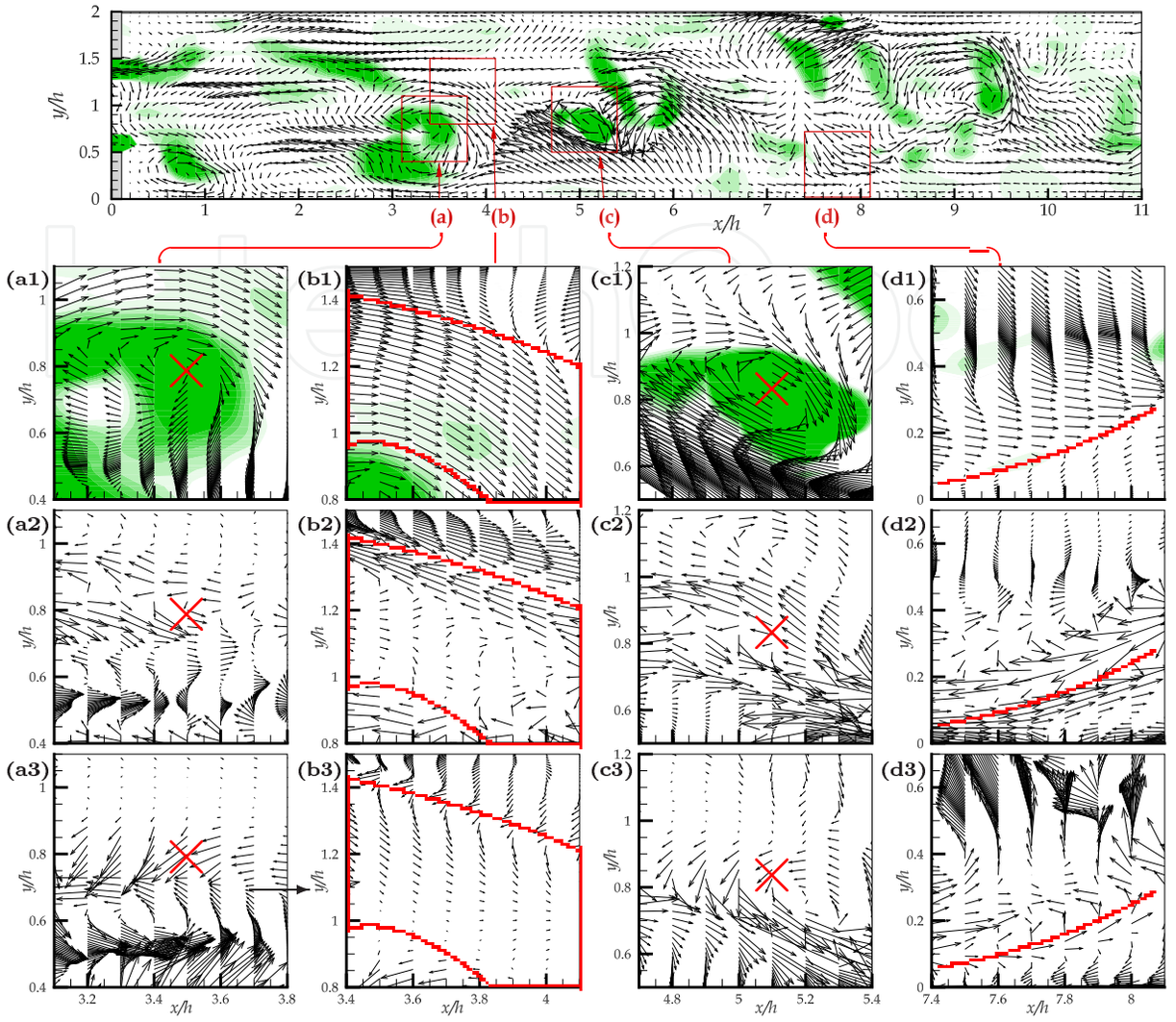

Figure 7. Instantaneous velocity-vector field of the viscoelastic flow, viewed in an arbitrary x-y plane. The main flow moves from left to right. Green contour denotes $II' \leq -0.005$. The small areas surrounded by red borders are shown in enlarged views of the following figures. (a–d) Enlarged views of the instantaneous field of the viscoelastic flow: (a1–d1), same as the top figure, the vector of u' and w' and the contour of $II' \leq -0.005$; (a2–d2) the vector denotes the force contributed by the viscous term (F_x, F_y); (a3–d3) the force by the viscoelastic term (E_x, E_y). The position of (a) focuses on a spanwise vortical motion near the orifice, and the symbol of ($\times$) indicates the vortex center: (b), another location in the core region without determinate vortical motion; (c), another vortical motion far from the orifice: (d), a near-wall turbulent motion (sweep and ejection) downstream of the reattachment point.

Regarding the facts that the K-H vortices as well as subsequent eddies were quickly damped but the quasi-streamwise vortices away from the orifice were sustained in the viscoelastic flow, we will consider these vortical motions in the frame of x-y plane and investigate their relationships to the conformation-stress (polymer or surfactant-micellar network stress) field.

4.2. Viscoelastic force exerted on fluid motions

As indicated in Fig. 7, four different small areas are chosen and compared with the vector patterns of the viscous and the viscoelastic body forcing terms in the governing equation

for the fluctuating velocity, namely, the second and third terms in the right-hand side of Equation (5) for u' and v':

$$\text{viscous force} \quad F_x = \frac{\beta}{Re_{\tau 0}} \frac{\partial^2 u'^+}{\partial x_j^{*2}} \ (\text{in } x), \quad F_y = \frac{\beta}{Re_{\tau 0}} \frac{\partial^2 v'^+}{\partial x_j^{*2}} \ (\text{in } y); \tag{9}$$

$$\text{viscoelastic force} \quad E_x = \frac{1-\beta}{We_{\tau 0}} \frac{\partial c_{xj}}{\partial x_j^*} \ (\text{in } x), \quad E_y = \frac{1-\beta}{We_{\tau 0}} \frac{\partial c_{yj}}{\partial x_j^*} \ (\text{in } y). \tag{10}$$

In Fig. 7(a), we extract a spanwise swirling motion that persist to a K-H vortex in a separated shear layer. As clearly described in Fig. 7(a1), the velocity vectors present a clockwise vortical motion and the contour of II' also implies the existence of an eddy. The distributions of viscous and viscoelastic force vectors are displayed in the successive figures, (a2) and (a3), respectively. It is clear that, the both force vectors show an anti-clockwise pattern that is opposite in direction to the fluid swirling, although the center of the viscoelastic force pattern deviate slightly from the center of the flow votex. The viscous force (F_x, F_y) is intensified (either positively or negatively) where the velocity gradient of $\mathrm{d}u/\mathrm{d}y$ drastically changes. The viscous force inherently inhibits the flow vortical motion.

As for a non-rotating fluid motion, shown in Figs. 7(b1) and (b2), the behavior of the viscous force field is similar to the rotating case. However, when compared to the distribution of (E_x, E_y), the flow in the core region without the shear of $\mathrm{d}u/\mathrm{d}y$ is found to be somewhat stimulated by the viscoelastic force: see the consistency in the direction of the force and velocity in the region enclosed by the red line in (b3). It may be relevant to the earlier findings that, away from the orifice ($x > 4.5h$), the mean velocity in the core region of the viscoelastic flow became significantly larger than that of the Newtonian flow: cf. Fig. 2 in the paper of [46] and Fig. 6 of [33]. The cause of the accelerated core flow is probably related to the extensional viscosity, the magnitude of which is accentuated by high levels of viscoelasticity but not varied for the Newtonian fluid. With the high extensional viscosity, the flow motion is hard to alter in the longitudinal direction. This effect should be responsible also for the attenuation of the Coanda effect that would cause the asymmetry in the mean flow past the orifice: for details to Section 6.

Next, let us consider the region away from the orifice. It is clearly seen in Fig. 6(c) that both (F_x, F_y) and (E_x, E_y) vectors oppose the velocity vector of (u', v') with respect to a spanwise vortex, as similar to the trend observed in (a). Considering the locations of upwelling and downwelling flows associated with the vortex, the distribution of (E_x, E_y) shows the viscoelastic force directly counteracting the fluid motions. The weakening of the spanwise vortices may also be attributed to this effect. It may be interesting to note that the anti-correlated swirling vector pattern of (E_x, E_y) is shifted slightly downstream with respect to the center of the swirling fluid motion. Such slight discordances between the velocity and viscoelastic force in terms of the rotational center are frequently observed not only in Fig. 6(a), but also other viscoelastic flows [15]. Further investigations are needed to clarify its cause and importance for the vortex retardation by viscoelasticity.

In the downstream of the reattachment point, quasi-streamwise vortices become more common than spanwise vortices, as seen in Fig. 6(b). Figure 7(d1) shows an impingement of the ejection (Q2) and the sweep (Q4) motions, the so-called 'bursting,' which generally occurs in the buffer layer of the wall turbulence. It is demonstrated that a quasi-streamwise vorticity

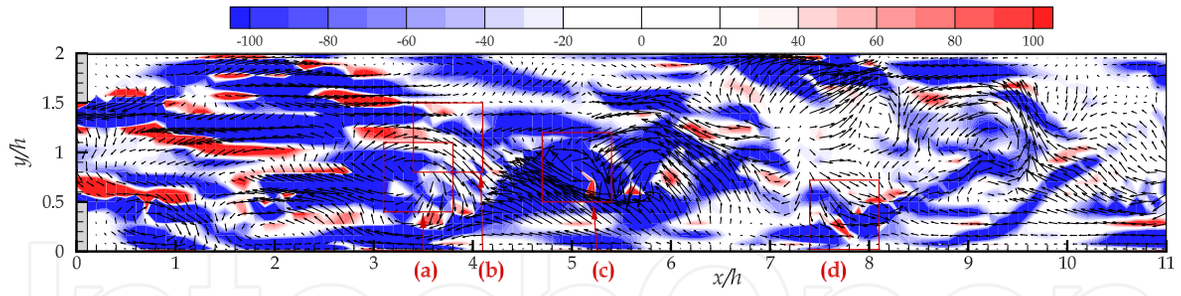

(a) Velocity (u, v) *versus* viscous force (F_x, F_y)

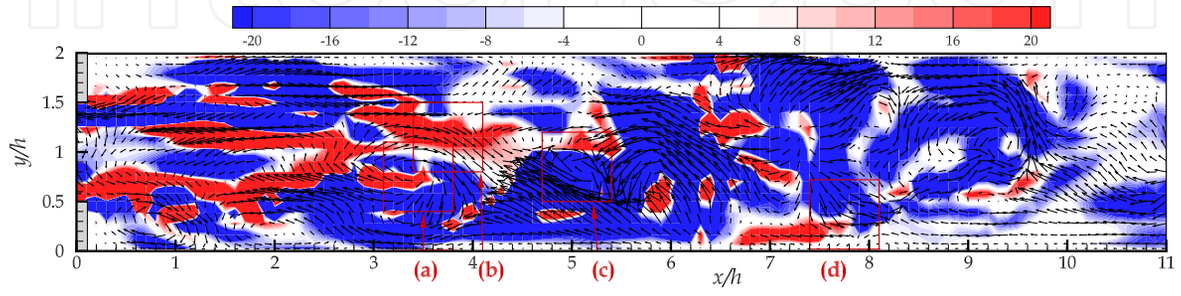

(b) Velocity (u, v) *versus* viscoelastic force (E_x, E_y)

Figure 8. Instantaneous distributions of the inner product of the velocity vector and the vector of either viscous force or the viscoelastic force, viewed in the same x-y plane and at the same instance with Fig. 7: (a) $\mathbf{u} \cdot \mathbf{F}$, (b) $\mathbf{u} \cdot \mathbf{E}$. The arrows represent the velocity vectors $\mathbf{u}$.

induces negative streamwise velocity fluctuations (below the red line in the figure), which results in a low-speed streak, and blowing down of high momentum fluid to the wall (above the red line). The vector fields of the viscous force and the viscoelastic force around them are shown in (d2) and (d3), respectively. Negative F_x is detected above the red line, where positive u' is induced, while positive F_x is observed very close to the wall. It is worth to note that this trend is not, however, consistent with the viscoelastic force (E_x, E_y) which has the almost same sign with (u', v') except for far from the wall, indicating that the viscoelastic force assists flow in some extent. This is presumably consistent with positive correlation between E_x and u' in the vicinity of the wall, as reported for the turbulence on smooth wall [1, 16].

4.3. Alignment between flow and force vectors

In order to see the variation in the relationship between the fluid motions and the viscoelastic force behaviors, we examine here the alignment between the flow vector and individual force. Figures 8(a) and (b) show the contour of the following inner product of two vectors—the velocity and either force of viscosity and viscoelasticity:

$$\mathbf{u} \cdot \mathbf{F} = |\mathbf{u}||\mathbf{F}| \cos \theta_F, \tag{11}$$

$$\mathbf{u} \cdot \mathbf{E} = |\mathbf{u}||\mathbf{E}| \cos \theta_E. \tag{12}$$

If the vectors of the flow and the viscous/viscoelastic force are parallel and have the same sign ($\theta_F,\ \theta_E \approx 0$), the contour is given with red in the contour. If they have the opposite sign ($\theta_F,\ \theta_E \approx \pi$), the contour becomes blue. Note that, when either velocity or force vector is negligible or their vectors align in perpendicular, the inner product should approach zero.

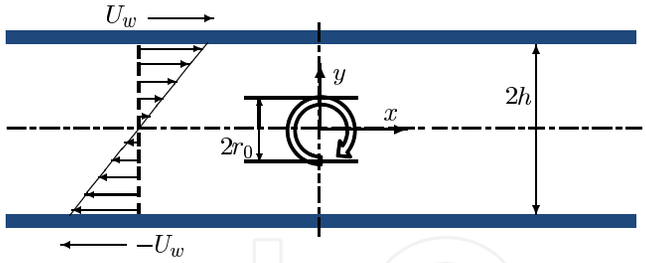

Figure 9. Initial field of laminar plane Couette flow with an immersed Rankine vortex.

As discussed in the preceding section, the plot of $\mathbf{u} \cdot \mathbf{E}$ in Fig. 8(b) shows that the viscoelastic force is anti-correlated with the spanwise vorticity just behind the orifice and in recirculation zone except for the core region. On the other hands, some consistency is observed in the near-wall region, but away from the reattachment point ($x > 6h$), where the sweep flows associated with the quasi-streamwise vortex motion are indeed confirmed to be stimulated by the viscoelastic force. As for the $\mathbf{u} \cdot \mathbf{F}$, Fig. 8(a) indicates that the viscous force inherently inhibits characterized fluid motions that we focus on here. The present concept of modification in vortical structures are qualitatively similar to those observed in the smooth wall-bounded turbulence [e.g., 6, 16].

Despite the rather phenomenological insight revealed by the above study, much further qualitative assessment should be required before understanding of the turbulent vortex modulation in the orifice flow for viscoelastic fluid is achieved.

5. Discussions

5.1. Simple test case: response to Rankine vortex in Couette flow

It would be instructive to examine the behavior of the viscoelastic body force in a simple test case, in the absence of any turbulent disturbance and downstream propagation. In this section, we investigate a localized spanwise eddy in a wall-bounded simple shear flow. In particular, the objective field is an incompressible plane Couette flow, which is driven by the relative movement of two parallel walls with the velocity of $\pm U_w$ (in x). The flow state is assumed to be basically laminar with a Reynolds number as low as $Re = \rho U_w h/\eta_0 = 60$, so that two-dimensional simulations have been performed both for Newtonian fluid and viscoelastic fluid. We focus on structures initially consisting of a Rankine-like vortex with its axis parallel to the z axis, no radial velocity ($u_r = 0$), and the tangential velocity of

$$u_\theta = \begin{cases} \Gamma r/(2\pi r_0^2) & (0 \le r \le r_0) \\ \Gamma/(2\pi r) & (r_0 < r) \end{cases}. \tag{13}$$

Here, (r, θ) and (u_r, u_θ) are the radial and circumferential coordinates and velocities that pertain to the vortex, respectively, r_0 the radius of the vortex, and Γ its circulation. While the gap between the walls is $2h$, the Rankine-line vortex with the diameter of $2r_0 = 0.4h$ was superimposed on the laminar Couette flow. The vortex center was set at the channel center, $y = 0$, so that the vortex would stay in position because of the net-zero bulk velocity. Figure 9 shows diagram of the flow configuration and the vortex, which has the rotational direction same with that of the mean flow vorticity. The governing equations and the relevant numerical scheme we used in this section were identical with those already introduced in Section 3. The

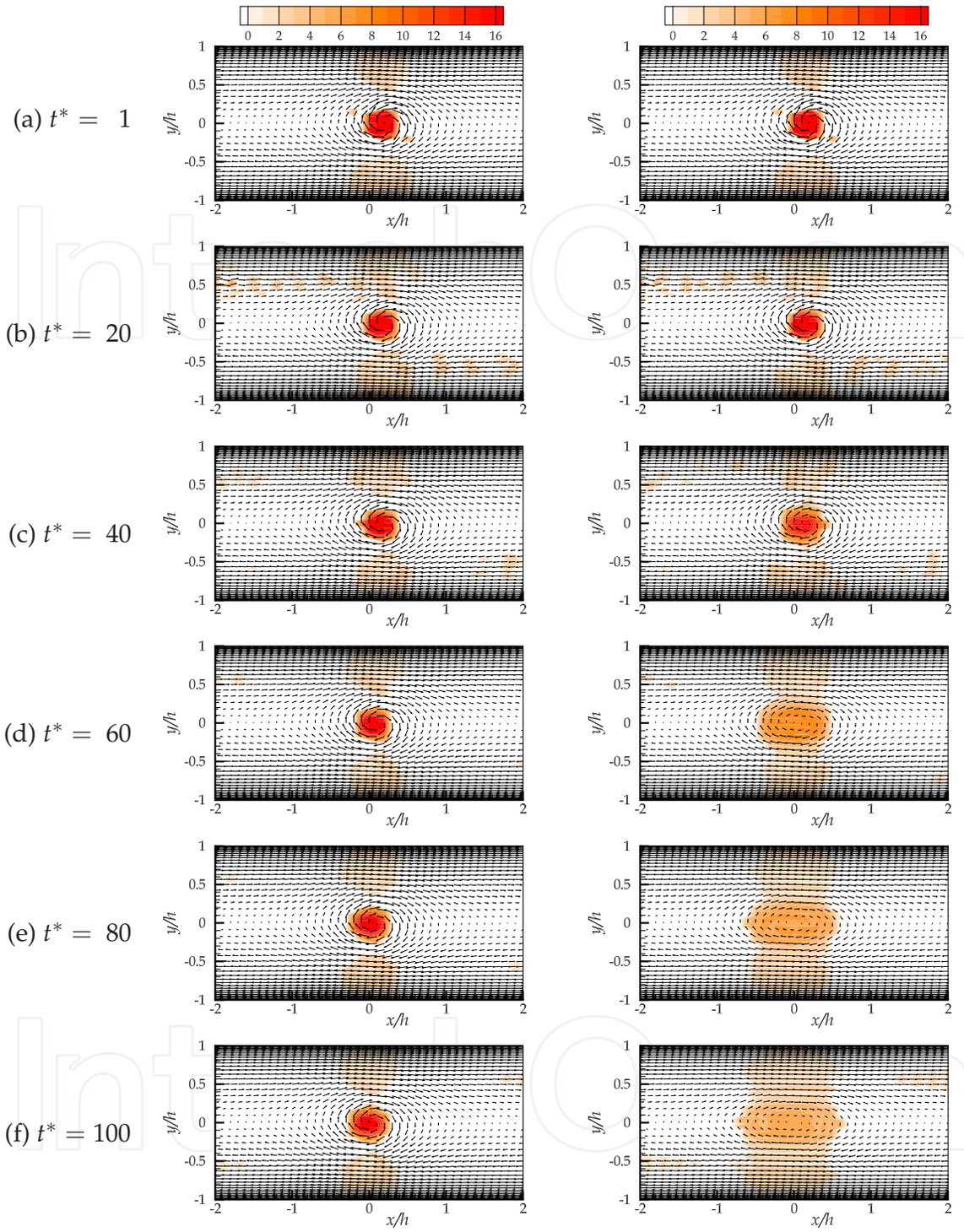

Figure 10. Temporal variation of a Rankin-like vortex in plane laminar Couette flow: (left-side column) Newtonian fluid, (right) viscoelastic fluid. Contour denotes the spanwise vorticity.

rheological parameters related to the Giesekus model were chosen as $We = \rho\lambda u_{\theta\max}^2/\eta_0 = 720$ ($u_{\theta\max}$ is comparable to U_w), $\beta = 0.8$, and $\alpha = 0.001$. The conformation tensor was initially given as zero at every point.

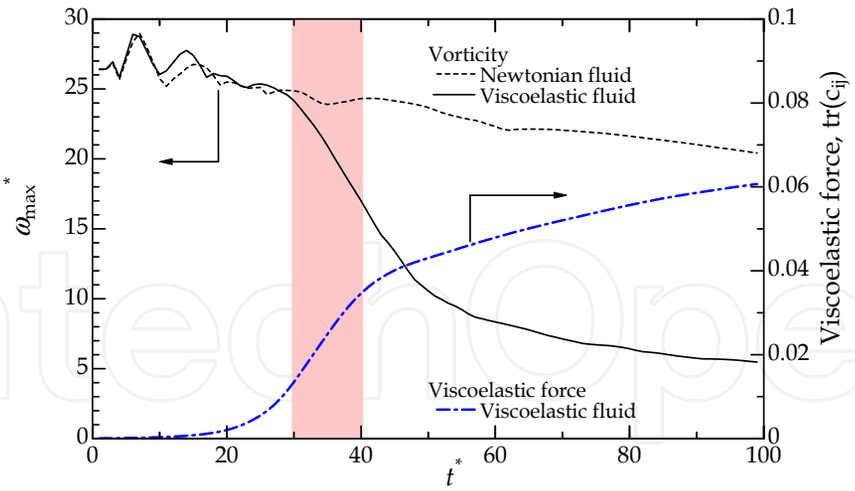

Figure 11. Time developments of the maximum vorticity at the vortex core and of the magnitude of the viscoelastic force.

The calculated vorticity and velocity fields show a rapid destruction, or decay, of the vortex in the viscoelastic fluid, which corresponds to the attenuation of spanwise K-H vortex shedding from the orifice edge. Figure 10 displays its decay process of the (clockwise) vortex for each fluid as a function of time, $t^* = tU_w/(2h)$. In the figure, the general flow pattern is characterized well by the swirling velocity vectors and seems to be not varied significantly in times, but their magnitude and the vorticity are remarkably reduced for $t^* = 40$–60 in the viscoelastic fluid flow. One may also observe that the vortex in this fluid is elongated along the mean flow, while the near-circular vortex stays in shape for the Newtonian fluid. This distortion is probably due to the high extensional viscosity of the viscoelastic fluid.

Figure 11 shows the temporal variation of the maximum vorticity (at the vortex center), $\omega_{\max}$, for each fluid and the included within the graph is the trace of viscoelastic stress, $c_{xx} + c_{yy} + c_{zz}$, as an indicator of viscoelastic force magnitude. In the initial stage of development, $\omega_{\max}$ fluctuates remarkably maybe because of the artificiality of the given initial flow field with immersed vortex, irrespective of the fluid. After that, both fluid flows are settled similarly for a while. From $t^* = 20$, the magnitude of viscoelastic-force becomes increased at an accelerated rate that exhibits some sort of peak during $t^* = 30$–40. A consequence of increased viscoelastic force is that the vortex has been attenuated significantly, as seen in the visualization of Fig. 10 and in Fig. 11. From $t^* = 50$, both of $\omega_{\max}$ and $\mathrm{tr}(c_{ij})$ take on somewhat moderate attitude: $\omega_{\max}$ gradually decreases as slowly as that for the Newtonian fluid; and $\mathrm{tr}(c_{ij})$ increases linearly, at least until $t^* = 100$. It is conjectured that the viscoelasticity acts to resist flow and obtain elastic energy from the kinetic energy of the vortex: this phenomenon is thought to occur as a delayed response with a lag that should be relevant to the fluid relaxation time λ.

To investigate further details of the relationship between the flow structure and the fluid viscoelasticity, we study the viscoelastic-force distribution as the way in which the turbulent orifice flow was analyzed in Section 4.3. Figure 12 shows streamlines for the viscoelastic flow at the same instances in time as given in Fig. 10. The background color map shows the inner product of the velocity vector and the viscoelastic body force, $\mathbf{u} \cdot \mathbf{E}$, as similar to the manner in Fig. 8. As already mentioned, the streamlines are practically unchanged or slightly distorted into the shape of an ellipse. It is interesting to note that the inner-product

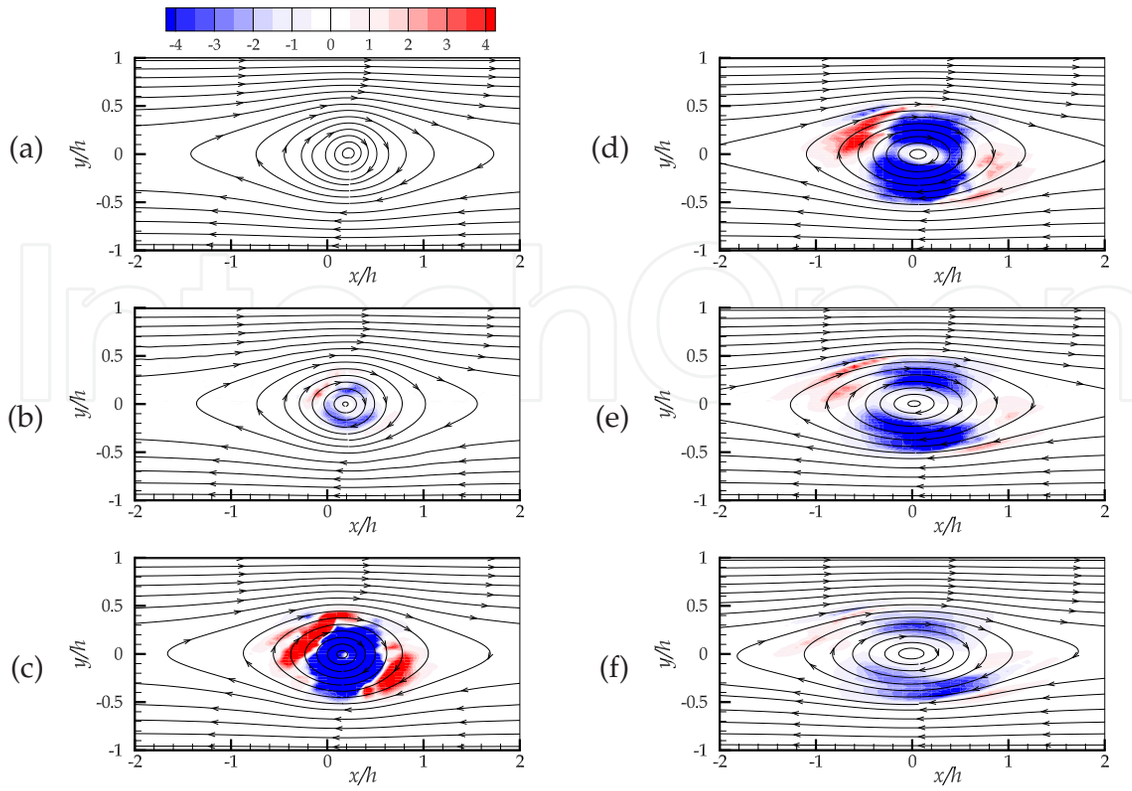

Figure 12. Streamlines and contour of the inner product of the velocity vector **u** and the viscoelastic force vector **E** at the same instance with Fig. 10 for the viscoelastic fluid.

distribution drastically alters in time and implies a mutual relation between the flow and viscoelasticity. If emphases are placed on the top-left and bottom-right parts with respect to the vortex center and on the top-right and bottom-left parts, a flow contraction and expansion, respectively, occur in gaps between each wall and the vortex. We find that the viscoelastic force in Fig. 12 assists flow in regions of strong extension (contraction) area around the vortex, where $\mathbf{u} \cdot \mathbf{E} > 0$, corresponding to red contour (see online version). On the other hand, most other parts of the vortex are found to be exerted resisting force mainly in regions of extension as well as the vortex core. Both these observations might be consistent with the trends observed in the orifice flow discussed earlier: that is, the wake past the orifice contraction would be sustained, whereas the expanding motion, or entrainment to the wall, be rather inhibited in viscoelastic fluid. These viscoelastic-fluid reaction can be confirmed to intensify during a finite time, in particular, $t^* = 30$–50 in the case of the present condition.

Although the vortex ranges in terms of size and magnitude and the relaxation time are not equivalent to those for the orifice flow discussed in Section 4, the concept of spanwise-vortex suppression should be, at least qualitatively, valid for those turbulent flows.

5.2. Vortex structures behind rib

Based on the discussions presented above, we propose a scenario of development of vortex structures and the difference between the two fluids. Figure 13 illustrates diagrams with emphasis on the Kelvin-Helmholtz vortices and successive longitudinal vortices. In the Newtonian fluid flow, the K-H vortices, which emanate from the edge of a rib and align

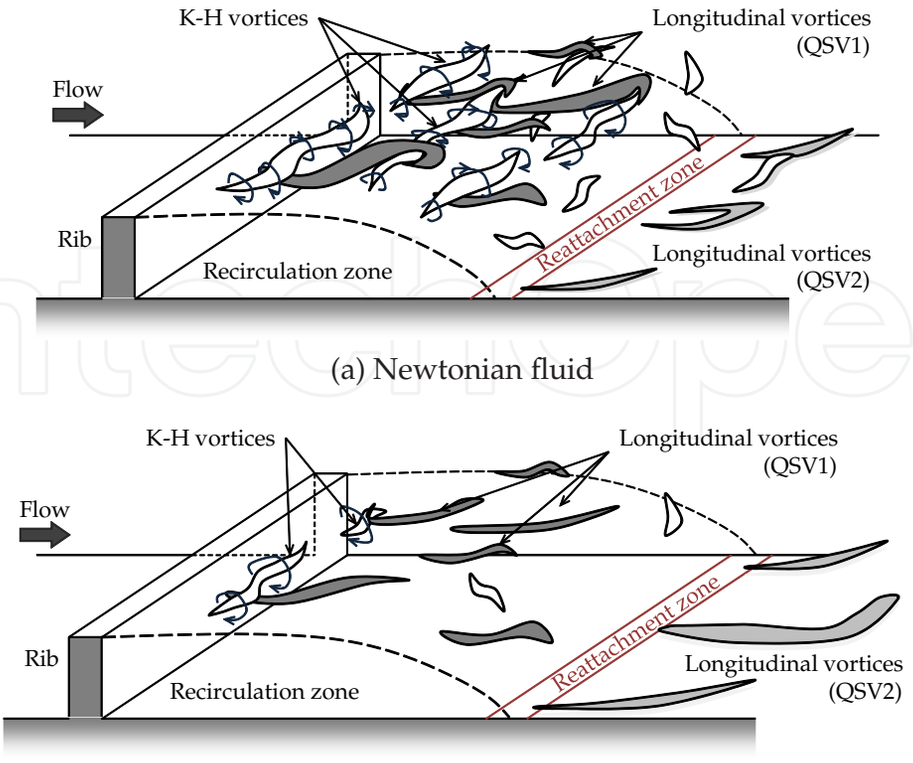

Figure 13. Conceptual scenario of the development of vortices in turbulent orifice flow for Newtonian fluid (a) and viscoelastic fluid (b).

parallel to the rib, propagate downstream with developing and inducing small eddies. Then, an intensive turbulent production arises above the reattachment zone. Moreover, once the three-dimensional disturbance reaches some finite amplitude, it produces a bending of spanwise K-H vortices and gives rise to additional eddies, the so-called *rib* vortices (labelled as QSV1 in the figure), extending in the streamwise direction, which bridge a sequence of the K-H vortices, as in the mixing layer [40]. Comte et al. [4] named this vortex pattern as a vortex-lattice structure, which was actually confirmed also in the present Newtonian orifice flow. In the downstream of the reattachment, quasi-streamwise vortices (QSV2) are expected to be dominant, as in the smooth channel flow. Basically, QSV1 and QSV2 may not the same structure in terms of generation process: the QSV1 should be generated in the separated shear layer and dissipated around the reattachment zone, while the QSV2 may be somewhat intensified structures of those observed in the smooth turbulent channel flow.

As demonstrated in Sections 4 and 5.1, spanwise vortices tend to be preferentially suppressed by the viscoelasticity, so that the K-H vortices rapidly decay, as schematically shown in Fig. 13(b). Accordingly, the longitudinal vortices (QSV1) become dominant structure but sparse even in a region above the recirculation and reattachment zone. The shift downstream of the reattachment zone occurs by the effect of viscoelasticity, as in agreement with the earlier experiments [29, 33]. This increase in the reattachment length inherently results in an expanse of the separated shear layer, i.e., the area of intensive turbulent production, in the downstream region. However, this expanded production area would not significantly contribute in regard to the net turbulent kinetic energy. For reference, the two-dimensional budget for the transport equation of the turbulent kinetic energy is presented in Section 6. In

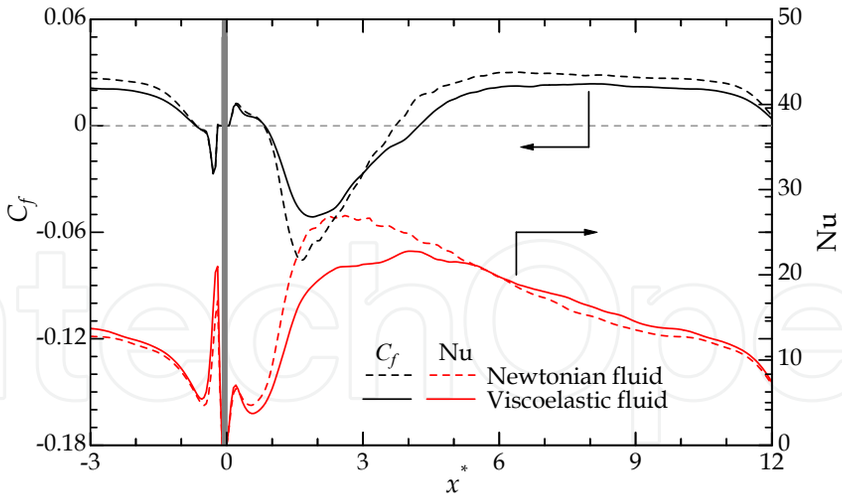

Figure 14. Comparison of Newtonian and viscoelastic flows in terms of streamwise distribution of local skin-frictional coefficient and Nusselt number. The orifice locates at $x^* = 0$–0.1. Cited from [49].

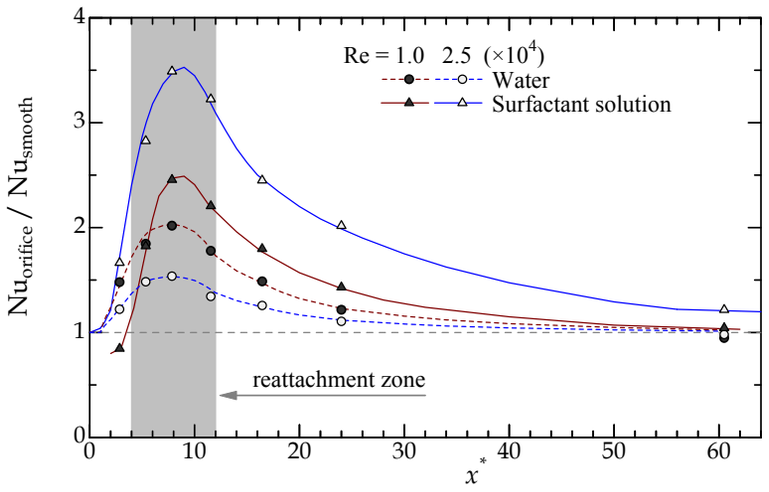

Figure 15. Experimental result for streamwise variations of the ratio between the local Nusselt number for the orifice flow and that for the smooth channel flow. The Reynolds number used here is based on the bulk mean velocity, the channel width $2h$, and the solvent kinematic viscosity. The orifice rear surface locates at $x^* = 0$. Cited from [13].

the downstream of the reattachment zone, much elongated QSV2 occurs and sustains for a longer period compared to that in the Newtonian flow. This is also a phenomenon affected by the fluid viscoelasticity, which is prone to assist some sort of elongational flows. It may be concluded that the viscoelastic flow would avoid rapid transition into turbulence just behind the orifice, whereas that flow be accompanied by long-life longitudinal vortices far downstream of the orifice.

5.3. Heat-transfer augmentation by orifice

In the context of above discussion on flow structures, their variations due to viscoelasticity are generally expected to significantly influence on heat and mass transfers. Better understanding of the thermal fields in the viscoelastic turbulent flow through complicated geometry is

practically important for their applications, such as heat exchanger working with coolant of polymer/surfactant solution liquids [37, 38].

For the purpose of briefly describing the phenomena characterized by heat-transfer augmentation/reduction in the viscoelastic orifice flow, the local Nusselt-number (Nu) profile as a function of x^* is plotted in Fig. 14. Here, a constant temperature difference between the top and bottom walls was adopted as for the thermal boundary condition, the other fluid conditions were same as those given in Section 2, and we numerically solved the energy equation for passive scalar with a constant Prandtl number of $Pr = 1.0$ in the absence of any temperature dependency. For details, please see our recent paper [49]. Contained within Fig. 14 is the local skin-frictional coefficient C_f. In a some extent behind the orifice, C_f is broadly negative until the reattachment point locating around $x^* = 4$, at which $C_f = 0$. In this region, both C_f and Nu are decreased in the viscoelastic flow, because turbulent motions as well as the K-H vortices are damped, as concluded in Section 5.2. This phenomenon corresponds to what is termed either DR (drag reduction) or HTR (heat-transfer reduction). It is noteworthy that, for the viscoelastic flow, Nu locally exceeds that for the Newtonian flow, while C_f keeps a lower value: see a range of $x^* = 6$–10 in Fig. 14. This implies a feasibility of highly-efficient heat exchanger with ribs that provides simultaneously heat-transfer enhancement and less momentum loss. We may presume that this paradoxical phenomenon is caused by the mutual interference between QSV2 and the fluid viscoelasticity.

We have also experimentally confirmed the fact that an orifice in the channel flow would significantly promote the heat transfer in its downstream, especially for the case of viscoelastic liquid [13]. The CTAC solution with 150 ppm was used as the test fluid. One of the channel walls was heated to maintain a constant temperature. As seen in Fig. 15, the installation of an orifice induced a drastic increase of Nu in and after the reattachment zone. This effect was found to be more pronounced for higher Reynolds numbers.

6. Conclusions

The effects of viscoelastic force on vortical structures in turbulent flow past the rectangular orifice have been numerically investigated. We confirmed that the viscoelastic force tended to play a role in the attenuation of spanwise vortices behind the orifice. As found in the viscoelastic turbulence through a smooth channel by Kim et al. [16], the counter viscoelastic force reduces the spanwise vortex strength by opposing the vortical motions, which may result in the suppression of the auto-generation of new spanwise vortices and intensive turbulence behind the orifice. On the other hands, in the downstream of the reattachment zone, the flows associated with the quasi-streamwise vortex motion are stimulated by the viscoelastic force. This may lead to longer life-time of longitudinal vortex and the heat-transfer augmentation in far downstream of the orifice, as compared to the Newtonian counterpart. It can be concluded that turbulent kinetic energy is transferred to the elastic energy through the vortex suppression, and the opposite exchange from the elastic energy to the turbulent kinetic energy occurs apart from the orifice.

Appendix: Several turbulence statistics

The streamlines of the mean flow for the viscoelastic fluid we dealt with in the present study and several turbulence statistics are given in Fig. 16. The turbulent intensities of u'^{+}_{rms}, v'^{+}_{rms},

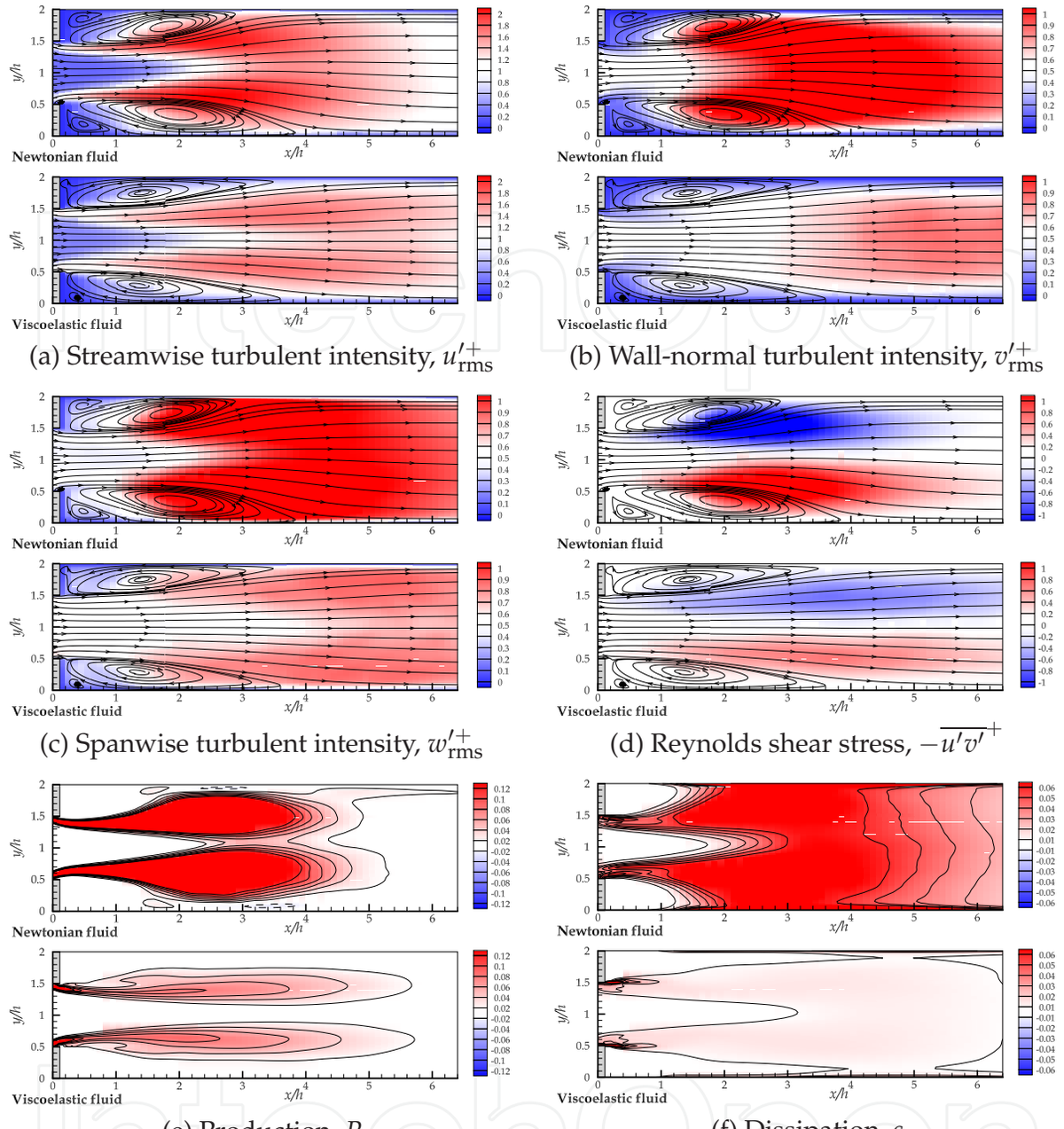

(a) Streamwise turbulent intensity, u'^{+}_{rms} (b) Wall-normal turbulent intensity, v'^{+}_{rms}

(c) Spanwise turbulent intensity, w'^{+}_{rms} (d) Reynolds shear stress, $-\overline{u'v'}^{+}$

(e) Production, P (f) Dissipation, ε

Figure 16. Mean-flow streamlines (a–d) and contours of various turbulence statistics: (a–c) turbulent intensities, (d) Reynolds shear stress, and (e, f) production and dissipation of turbulent kinetic energy. Note that ranges of accompanying color bars are different in each figure. For each statistic, the Newtonian flow and the viscoelastic flow are presented in the upper and lower figures, respectively. The budget terms in (e, f) are non-dimensionalized by $\rho u_{\tau 0}^4/\eta_0$.

and w'^{+}_{rms} represent the root-mean-square of velocity fluctuation in the x, y, and z direction, respectively. Only a major Reynolds shear stress of $-\overline{u'v'}^{+}$ is also shown in Fig. 16(d).

The balance equation for the turbulent kinetic energy $k = \overline{u_i' u_i'}/2$ in a fully-developed flow can be expressed as

$$\frac{\mathrm{d}k}{\mathrm{d}t} = P - \varepsilon + D^p + D^t + D^\nu + A + E = 0, \tag{14}$$

where

$$\text{production,} \quad P = -\overline{u_i' u_k'} \frac{\partial U_i}{\partial x_k}; \tag{15}$$

$$\text{dissipation,} \quad \varepsilon = \frac{\eta_s}{\rho} \overline{\frac{\partial u_i'}{\partial x_k} \frac{\partial u_i'}{\partial x_k}}; \tag{16}$$

D^p, D^t, and D^v, the diffusion terms by pressure, turbulence, and viscous, respectively; A, the advectional contribution; and E, the viscoelastic contribution. An overbar and capital letter represent average values: U, the streamwise mean velocity. Figures 16(e) and (f) show in-plane distributions of P and ε in a range of $x^* \in [0, 6.4]$ and $y^* \in [0, 2]$.

From the results given in Fig. 16, we have obtained the following insights: (1) the viscoelastic fluid would provide rather symmetric streamlines with respect to the channel center, while the asymmetry due to the Coanda effect occurs clearly despite the symmetric geometry, (2) the intensive turbulence region as well as the turbulence-producing area at the separated shear layer are shifted downstream in the viscoelastic fluid, (3) the suppression of the Kelvin-Helmholtz vortices results in a significant reduction in v'^{+}_{rms} just behind the orifice, and (4) the region where relatively high dissipation occurs shifted far downstream as similar to the turbulence-producing area.

For further information, one may refer to [46], although a detailed discussion including analysis of the energy/stress budget will be presented in the near future.

Acknowledgements

All of the present DNS computations were carried out with the use of supercomputing resources of Cyberscience Center at Tohoku University and those of Earth-Simulator Center of JAMSTEC (Japan Agency for Marine-Earth Science and Technology). We also gratefully acknowledge the assistances of our Master's course student at Tokyo University of Science: Mr. Tomohiro Kawase for his exceptional works in DNS operation; and Mr. Daisei Tsurumi and Ms. Shoko Kawada for their contribution to the experimental part of this study. The authors would like to thank Prof. H. Kawamura, President of Tokyo University of Science, Suwa, for stimulating discussions.

This chapter is a revised and expanded version of a paper entitled "Numerical investigation of viscoelastic effects on turbulent flow past rectangular orifice," presented at the 22nd International Symposium on Transport Phenomena [47].

Author details

Takahiro Tsukahara and Yasuo Kawaguchi
Tokyo University of Science, Japan

7. References

[1] de Angelis, E., Casciola, C.M., & Piva, R. (2002). DNS of wall turbulence: Dilute polymers and self-sustaining mechanisms, *Computers & Fluids*, Vol. 31, 495–507.

[2] Armaly, B.F., Durst, F., Pereira, J.C.F., & Schönung, B. (1983). Experimental and theoretical investigation of backward-facing step flow, *Journal of Fluid Mechcanics*, Vol. 127, 473–496.
[3] Castro, O.S. & Pinho, F.T. (1995). Turbulent expansion flow of low molecular weight shear-thinning solutions, *Experiments in Fluids*, Vol. 20, 42–55.
[4] Comte, P., Lesieur, M., & Lamballais, E. (1992). Large- and small-scale stirring of vorticity and a passive scalar in a 3-D temporal mixing layer, *Physics of Fluid A*, Vol. 4, 2761–2778.
[5] Dales, C., Escudier, M.P., & Poole, R.J. (2005). Asymmetry in the turbulent flow of a viscoelastic liquid through an axisymmetric sudden expansion, *Journal of Non-Newtonian Fluid Mechanics*, Vol. 125, 61–70.
[6] Dubief, Y., White, C.M., Terrapon, V.E., Shaqfeh, E.S.G., Moin, P., & Lele, S.K. (2004). On the coherent drag-reducing and turbulence-enhancing behaviour of polymers in wall flows, *Journal of Fluid Mechanics*, Vol. 514, 271–280 .
[7] Dimitropoulos, C.D., Sureshkumar, R., Beris, A.N., & Handler, R.A. (2001). Budgets of Reynolds stress, kinetic energy and streamwise enstrophy in viscoelastic turbulent channel flow, *Physics of Fluids*, Vol. 13, 1016–1027.
[8] Escudier, M.P. & Smith, S. (1999). Turbulent flow of Newtonian and shear-thinning liquids through a sudden axisymmetric expansion. *Experiments in Fluids*, Vol. 27, 427–434.
[9] Fadlun, E.A., Verzicco, R., Orlandi, P., & Mohd-Yusof, J. (2000). Combined immersed-boundary finite-difference methods for three-dimensional complex flow simulations, *Journal of Computational Physics*, Vol. 161, 35–60.
[10] Giesekus, H. (1982). A simple constitutive equation for polymer fluids based on the concept of deformation-dependent tensorial mobility, *Journal of Non-Newtonian Fluid Mechanics*, Vol. 11, 69–109.
[11] Gyr, A. & Bewersdorff, H.-W. (1995). *Drag reduction of turbulent flows by additives*, Kluwer Academic Publisher, ISBN 978-90-481-4555-3, Dordrecht.
[12] Joseph, D.D. (1990). *Fluid dynamics of viscoelastic liquids*, Springer-Verlag, ISBN 978-0387971551, New York.
[13] Kawada, S., Tsurumi, D., Kawase, T., Tsukahara, T., & Kawaguchi, Y. (2012). Experimental study on heat transfer augmentation in viscoelastic turbulent channel flow by two-dimensional orifice, In: *Turbulent, Heat and Mass Transfer 7*, Begell House, Inc., in press.
[14] Kawaguchi, Y., Wei, J.J., Yu, B., & Feng, Z.P. (2003). Rheological characterization of drag-reducing cationic surfactant solution: shear and elongational viscosities of dilute solutions, *Proceedings of ASME/JSME 2003 4th Joint Fluids Summer Engineering Conference* , pp. 721–728, Honolulu, Hawaii, USA, July 6–10, 2003.
[15] Kim, K., Li, C.-F., Sureshkumar, R, Balachandar, S., & Adrian, R.J. (2007). Effects of polymer stresses on eddy structures in drag-reduced turbulent channel flow, *Journal of Fluid Mechcanics*, Vol. 584, 281–299.
[16] Kim, K., Adrian, R.J., Balachandar, S., & Sureshkumar, R. (2008). Dynamics of hairpin vortices and polymer-induced turbulent drag reduction, *Physical Review Letter*, Vol. 100, 134504, 4 pp.
[17] Li, C.-F., Sureshkumar, R., & Khomami, B. (2006). Influence of rheological parameters on polymer induced turbulent drag reduction, *Journal of Non-Newtonian Fluid Mechcanics*, Vol. 140, 23–40.
[18] Li, F.-C., Yu, B., Wei, J.J. & Kawaguchi, Y. (2012). *Turbulent drag reduction by surfactant additives*, John Wiely & Sons, Inc., ISBN 978-1-118-18107-2, Singapore.
[19] Lumley, J.L. (1969). Drag reduction by additives, *Annual Review of Fluid Mechanics*, Vol. 1, 367–384.

[20] L'vov, V.S., Pomyalov, A., Procaccia, I., & Tiberkevich, V. (2004). Drag reduction by polymers in wall-bounded turbulence, *Physical Review Letter*, Vol. 92, 244503, 4 pp.
[21] Manica, R. & De Bortoli, A.L. (2004). Simulation of sudden expansion flows for power-law fluids. *Journal of Non-Newtonian Fluid Mechanics*, Vol. 121, 35–40.
[22] Makino, S., Iwamoto, K., & Kawamura, H. (2008a). Turbulent structures and statistics in turbulent channel flow with two-dimensional slits, *International Journal Heat and Fluid Flow*, Vol. 29, 602–611.
[23] Makino, S., Iwamoto, K., & Kawamura, H. (2008b). DNS of turbulent heat transfer through two-dimensional slits, *Progress in Computational Fluid Dynamics*, Vol. 8, 397–405.
[24] Mohd-Yusof, J. (1998). Development of immersed boundary methods for complex geometries, *Center for Turbulence Research Annual Research Briefs 1998*, NASA Ames, Stanford University, 325–336.
[25] Motier, J.F. & Carrier, A.M. (1989). Recent studies in polymeric drag reduction in commercial pipelines. *Drag reduction in fluid flows: techniques for friction control*, eds. Sellin, R.H.J. & Moses, R.T., Halsted Press, New York, 197–204.
[26] Nadolink, R.H. & Haigh, W.W. (1995). Bibliography on skin friction reduction with polymers and other boundary-layer additives, *Applied Mechanics Reviews*, Vol. 48, 351–460.
[27] Nie, J.H. & Armaly, B.F. (2004). Reverse flow regions in three-dimensional backward-facing step flow. *International Journal of Heat and Mass Transfer*, Vol. 47, 4713–4720.
[28] Oliveira, P.J. (2003). Asymmetric flows of viscoelastic fluids in symmetric planar expansion geometries. *Journal of Non-Newtonian Fluid Mechanics*, Vol. 114, 33–63.
[29] Pak, B., Cho, Y.I., & Choi, S.U.S. (1990). Separation and reattachment of non-newtonian fluid flows in a sudden expansion pipe. *Journal of Non-Newtonian Fluid Mechanics*, Vol. 37, 175–199.
[30] Peskin, C.S. (1977). Numerical analysis of blood flow in the heart. *Journal of Computational Physics*, Vol. 25, 220–252.
[31] Poole, R.J. & Escudier, M.P. (2003a). Turbulent flow of non-Newtonian liquids over a backward-facing step: Part II. Viscoelastic and shear-thinning liquids, *Journal of Non-Newtonian Fluid Mechanics*, Vol. 109, 193–230.
[32] Poole, R.J. & Escudier, M.P. (2003b). Turbulent flow of a viscoelastic shear-thinning liquid through a plane sudden expansion of modest aspect ratio, *Journal of Non-Newtonian Fluid Mechanics*, Vol. 112, 1–26.
[33] Poole, R.J. & Escudier, M.P. (2004). Turbulent flow of viscoelastic liquids through an asymmetric sudden expansion, *Journal of Non-Newtonian Fluid Mechanics*, Vol. 117, 25–46.
[34] Poole, R.J., Alves, M.A., Oliveira, P.J., & Pinho, F.T. (2007). Plane sudden expansion flows of viscoelastic liquids, *Journal of Non-Newtonian Fluid Mechanics*, Vol. 146, 79–91.
[35] Procaccia, I., L'vov, V.S., & Benzi, R. (2008). Colloquium: Theory of drag reduction by polymers in wall-bounded turbulence, *Reviews of Modern Physics*, Vol. 80, 225–247.
[36] Prosperetti, A. & Tryggvason, G. (2007). *Computational methods for multiphase flow*, Cambridge University Press, ISBN 978-0-521-84764-3, Cambridge.
[37] Qi, Y., Kawaguchi, Y., Lin, Z., Ewing, M., Christensen, R.N., & Zakin, J.L. (2001). Enhanced heat transfer of drag reducing surfactant solutions with fluted tube-in-tube heat exchanger, *International Journal Heat and Mass Transfer*, Vol. 44, 1495–1505.
[38] Qi, Y., Kawaguchi, Y., Christensen, R.N., & Zakin, J.L. (2003). Enhancing heat transfer ability of drag reducing surfactant solutions with static mixers and honeycombs, *International Journal Heat and Mass Transfer*, Vol. 46, 5161–5173.

[39] Roy, A., Morozov, A., van Saarloos, W., & Larson, R.G. (2006). Mechanism of polymer drag reduction using a low-dimensional model, *Physical Review Letter*, Vol. 97, 234501, 4pp.
[40] Schmid, P.J. & Henningson, D.S. (2001). *Stability and Transition in Shear Flows*, Springer-Verlag, ISBN 978-0-387-98985-3, New York.
[41] Sureshkumar, R. & Beris, A.N. (1995). Effect of artificial stress diffusivity on the stability of numerical calculations and the flow dynamics of time-dependent viscoelastic flows, *Journal of Non-Newtonian Fluid Mechanics*, Vol. 60, 53–80.
[42] Suzuki, H., Ishihara, K., & Usui, H. (2001). Numerical study on a drag reducing flow with surfactant additives, *Proceedings of 3rd Pacific Rim Conference on Rheology*, Paper No. 019, Vancouver, Canada, 8–13 July, 2001.
[43] Takeuchi, H. (2012). Demonstration test of energy conservation of central air conditioning system at the Sapporo City Office Building., *Synthesiology, English edition*, Vol. 4, 136–143.
[44] den Toonder, J.M.J., Hulsen, M.A., Kuiken, G.D.C., & Nieuwstadt, F.T.M. (1997). Drag reduction by polymer additives in a turbulent pipe flow: numerical and laboratory experiments, *Journal of Fluid Mechanics*, Vol. 337, 193–231.
[45] Tsukahara, T., Ishigami, T., Yu, B., & Kawaguchi, Y. (2011a). DNS study on viscoelastic effect in drag-reduced turbulent channel flow, *Journal of Turbulence*, Vol. 12, No. 13, 13 pp.
[46] Tsukahara, T., Kawase, T., & Kawaguchi, Y. (2011b). DNS of viscoelastic turbulent channel flow with rectangular orifice at low Reynolds number, *International Journal of Heat and Fluid Flow*, Vol. 32, 529–538.
[47] Tsukahara, T., Kawase, T., & Kawaguchi, Y. (2011c). Numerical investigation of viscoelastic effects on turbulent flow past rectangular orifice, In: *Proceedings of the 22nd International Symposium on Transport Phenomena*, Paper #129 (USB), 7pp., Delft, The Netherlands, 8–11 November 2011.
[48] Tsukahara, T. & Kawaguchi, Y. (2011). Turbulent heat transfer in drag-reducing channel flow of viscoelastic fluid, *Evaporation, Condensation and Heat transfer* (ed., A. Ahsan), InTech, Rijeka, Croatia, pp. 375-400.
[49] Tsukahara, T. & Kawaguchi, Y. (2012). DNS on turbulent heat transfer of viscoelastic fluid flow in a plane channel with transverse rectangular orifices, *Progress in Computational Fluid Dynamics*, in press.
[50] Tsurumi, D., Kawada, S., Kawase, T., Tsukahara, T., & Kawaguchi, Y. (2012). Experimental analysis of turbulent structure of viscoelastic fluid flow in downstream of two-dimensional orifice. In: *Turbulent, Heat and Mass Transfer 7*, Begell House, Inc., in press.
[51] White, C.M. & Mungal, M.G. (2008). Mechanics and prediction of turbulent drag reduction with polymer additives, *Annual Review Fluid Mechacnics*, Vol. 40, 235–256.
[52] Yu, B. & Kawaguchi, Y. (2004). Direct numerical simulation of viscoelastic drag-reducing flow: a faithful finite difference method, *Journal of Non-Newtonian Fluid Mechanics*, Vol. 116, 431–466.
[53] Yu, B., Li, F., & Kawaguchi, Y. (2004). Numerical and experimental investigation of turbulent characteristics in a drag-reducing flow with surfactant additives, *International Journal of Heat and Fluid Flow*, Vol. 25, 961–974.
[54] Zakin, J.L., Myska, J., & Chara, Z. (1996). New limiting drag reduction and velocity profile asymptotes for nonpolymeric additives systems, *AIChE Journal*, Vol. 42, 3544–3546.